



Microstructure evolution during tempering of martensitic Fe–C–Cr alloys at 700 °C

Ziyong Hou^{1,2,*} , R. Prasath Babu¹ , Peter Hedström¹ , and Joakim Odqvist¹ 

¹Department of Materials Science and Engineering, KTH Royal Institute of Technology, 100 44 Stockholm, Sweden

²State Key Laboratory of Rolling and Automation, Northeastern University, Shenyang 110819, Liaoning Province, People's Republic of China

Received: 2 September 2017

Accepted: 13 January 2018

Published online:
25 January 2018

© The Author(s) 2018. This article is an open access publication

ABSTRACT

The microstructure evolution of two martensitic alloys Fe–0.15C–(1.0 and 4.0) Cr (wt%) was investigated, using X-ray diffraction, electron backscatter diffraction, electron channeling contrast imaging and transmission electron microscopy, after interrupted tempering at 700 °C. It was found that quenching of 1-mm-thick samples in brine was sufficient to keep most of the carbon in solid solution in the martensite constituent. The high dislocation density of the martensite decreased rapidly during the initial tempering but continued tempering beyond a few minutes did not further reduce the dislocation density significantly. The initial martensitic microstructure with both coarse and fine laths coarsened slowly during tempering for both alloys. However, a clear difference between the two alloys was distinguished by studying units separated by high-angle boundaries (HABs). In the low-Cr alloy, M₃C precipitates formed and coarsened rapidly, thus they caused little hindrance for migration of HABs, i.e., coarsening of the HAB units. On the other hand, in the high-Cr alloy, M₇C₃ precipitates formed and coarsened slowly, thus they were more effective in pinning the HABs than M₃C in the low-Cr alloy, i.e., coarsening of HAB units was minute in the high-Cr alloy.

Introduction

As one of the main strengthening constituents in high-performance steels, martensite has been attracting significant attention. The martensitic microstructure with high defect density and units arranged in different hierarchic levels is complex and can be considered to be a low-ductility microstructure. Therefore, it must in general undergo a

tempering treatment to improve the toughness before it is put to use [1, 2]. The tempering of martensite has been investigated for a long time, and the development of transition carbides and cementite as well as defect annihilation during tempering of martensitic carbon steels is well known [3–12]. However, when it comes to highly alloyed steels that are tempered at high temperatures, the literature is scarce [13–15]. It is in particular difficult to find quantitative studies on

Address correspondence to E-mail: ziyong@kth.se

the evolution of different microstructural parameters such as the evolution of the size distribution of laths [1] during tempering of alloyed steels.

Fe–C–Cr is the base system for important steel categories such as hot-work tool steels. Further developments of these steels rely on an improved understanding of the microstructural evolution during tempering and subsequent service which, in general, occurs at a somewhat lower temperature than the tempering treatment. Therefore, it is essential to gain an understanding of softening of the martensitic matrix by defect annihilation and microstructural coarsening, but it is also quite important to understand the precipitation of carbides during tempering. To retain their hot hardness, these steels often rely on a multistage precipitation sequence where the formation of different transition metal carbides at different points in time during service enables preservation of the hardness [1–3]. Recent improvements in theoretical and experimental analysis of steels, inspired by the trend toward integrated computational materials engineering (ICME) [16], enable more computationally driven development of tempered martensite. However, further improvements in the predictive capabilities of models predicting microstructure and correlating with properties rely on an improved understanding of the microstructure evolution during tempering. The modeling of precipitation must consider the different potency of nucleation sites and the diffusional mobilities in the bulk and through crystal defects, including their evolution during tempering. Furthermore, models correlating structure and properties must be able to predict both the potential precipitation hardening effect and how this is counteracted by softening of the matrix which occurs by defect annihilation and carbon migration.

The purpose of the present work was, therefore, to investigate the microstructure evolution of martensitic Fe–C–Cr alloys during tempering. Two model alloys both resulting in a lath martensitic microstructure [17], with varying additions of chromium—a slow diffusing substitutional element compared to carbon, were investigated. The evolution of the martensitic microstructure and precipitation during tempering was evaluated using X-ray diffraction (XRD), electron backscatter diffraction (EBSD), electron channeling contrast imaging (ECCI) and transmission electron microscopy (TEM). The

effect of varying Cr composition on the evolution of the microstructure is discussed.

Experimental methods

The chemical compositions of the steels studied are listed in Table 1, and the preparation procedures for these alloys can be seen elsewhere [17]. The M_s temperatures were calculated using the model proposed by Stormvinter et al. [18] and are also listed in Table 1. The ternary Fe–C–Cr alloy samples ($10 \times 10 \times 1$ mm) were austenitized at 1100 °C for 10 min, followed by quenching in brine to room temperature. Thereafter, the quenched specimens were tempered at 700 °C for 5 s, 5 min, 30 min and 5000 h and immediately quenched to room temperature in order to follow the microstructure evolution during tempering. To eliminate the influence of the heating time, short-duration tempering treatments (5 s and 5 min) were performed in a Sn–Bi metal bath, whereas the longer heat treatments were performed in an argon atmosphere in a tube furnace (30 min). The sample tempered for 5000 h at 700 °C was vacuum encapsulated in a quartz tube and intended to be used as a reference sample.

Measurements of dislocation densities and lattice parameters were performed using XRD. Prior to XRD measurements, all specimens were polished mechanically and electrolytically to make sure that no strain was introduced into the sample surface during metallographic sample preparation. The measurements were performed using a Bruker D8 Discover instrument in Bragg–Brentano geometry using Cu–K α radiation. The diffraction patterns were recorded from 40° to 145° 2θ with angular steps of 0.01° and a counting time of 6 s per step. The diffraction peaks 110, 200, 211, 220, 310 and 222 were used in the subsequent analysis. No retained austenite was found by XRD in the as-quenched microstructure. The background and the Cu – K α_2 signals were subtracted from the diffraction patterns prior to further analysis. Least-square fitting of a pseudo-Voigt function was applied to find the peak centers and the full width at half maximum (FWHM). The instrumental peak broadening was evaluated using an Al $_2$ O $_3$ reference sample, and it was subtracted from the measured peak width. A polynomial function was applied to fit the peak broadening with respect to the 2θ angle [19]. A combination of the

Table 1 Chemical composition of the investigated alloys (in wt%), and the corresponding calculated Ms temperature using the model proposed in Ref. [18]

| Samples | C | Cr | Si | Mn | S | Al | Cu | Ni | Ms [°C] |
|-------------|------|-------|-------|------|------|-------|-------|-------|---------|
| 0.15C–1.0Cr | 0.14 | 0.983 | 0.021 | 0.07 | 0.06 | 0.014 | 0.011 | 0.017 | 465 |
| 0.15C–4.0Cr | 0.16 | 4.05 | 0.028 | 0.08 | 0.05 | 0.02 | 0.009 | 0.015 | 408 |

modified Williamson–Hall (MWH) and modified Warren–Averbach (MWA) methods was used to evaluate the dislocation densities. The analysis procedure presented in Refs. [20–22] was adopted and further details can be found there. The tetragonality of the martensite obtained was evaluated by considering the ratio between the 310 and 222 peaks [2, 23]. The c/a ratio obtained in both the as-quenched and the reference conditions was unity, within the error margins obtained, and thus the structure was treated as BCC. The lattice parameter was calculated from the d-spacing of the 222 peak and used to evaluate the carbon content of the matrix for the different conditions. The reference sample, tempered for 5000 h at 700 °C, was used to estimate the lattice parameter of the matrix at equilibrium carbon content. Then, the difference in lattice parameter (Δa [Å]) with respect to the equilibrium lattice parameter gave the solute carbon levels (C) in wt%, in accordance with [23]:

$$C = 31 \times \Delta a \quad (1)$$

Samples for SEM analyses were prepared by mechanical grinding and polishing, finishing with an alumina slurry with a particle size of 0.05 µm. ECCI images were acquired in randomly selected grains for the evaluation of lath size. The thickness of the laths was evaluated with a linear intercept method using lines drawn perpendicular to the length direction of the laths. For each sample, more than 600 laths in several locations were counted to provide sufficient statistics. Orientation maps obtained through automated EBSD was also utilized to study the hierarchic structure of fresh and tempered martensite. Both EBSD and ECCI measurements were performed using a JEOL JSM-7800F field-emission SEM operated at 15 kV. The EBSD analysis was acquired using a Bruker e-flash^{HR} detector, the scan step size was either 50 or 100 nm, and data acquisition and post-processing were performed using the Bruker Quantax software.

The SEM analysis was complemented by TEM analysis to evaluate the microstructure and to identify the precipitates that formed. The TEM analysis was conducted using a JEOL JEM-2100F microscope, equipped with energy-dispersive X-ray spectroscopy (EDS) and operating at 200 kV. TEM samples were prepared using the carbon extraction replica technique. Further details can be found in Ref. [24]. Thin-foil TEM samples were also prepared from the as-quenched and tempered samples for the analysis of the microstructure. The thickness of the laths was measured from TEM micrographs using a similar linear intercept method as employed in SEM-ECCI. The TEM lath thickness measurements were relatively less statistically populated since the idea was to compare and validate the SEM-ECCI measurements. To quantitatively analyze the precipitates, all the precipitates were assumed to be spherical and the number density of precipitates was evaluated using the equation:

$$N_d = \frac{N_p}{A} \quad (2)$$

where N_p is the number of precipitates in the measured area A .

Results and discussion

Dislocation density evolution from X-ray diffraction measurements

An example of the XRD pattern for the as-quenched 0.15C–4.0Cr alloy is shown in Fig. 1. In Fig. 1a, BCC martensite peaks and a representative 211 diffraction peak fitted using a pseudo-Voigt function are shown. The intensities of the peaks increase and the widths of the peaks decrease significantly already after 5-s tempering at 700 °C, see example in Fig. 1b. The same behavior was found for the 0.15C–1.0Cr alloy.

Figure 2 shows the peak broadening of all the BCC peaks for the as-quenched and tempered conditions

of alloys 0.15C–4.0Cr (Fig. 2a) and 0.15C–1.0Cr (Fig. 2b). The peak broadening is given by $\Delta K = \cos \theta (2\Delta\theta)/\lambda$ [19, 21, 22], where λ is the wavelength of the Cu – K_{α_1} X-rays (0.15406 nm), and $2\Delta\theta$ is the FWHM. It is clear that the peak broadening decreases rapidly during the initial 5 s of tempering and thereafter the rate of change is lower.

The dislocation density evolution during tempering in both alloys is shown in Fig. 3a. It should be noted that other types of defects such as twins were assumed to not contribute to the peak broadening. The dislocation density evolution shown in Fig. 3a is in good qualitative agreement with data reported in the literature for martensitic microstructures in ferrous systems [10, 14]. It can be seen that the dislocation density in alloys 0.15C–4.0Cr and 0.15C–1.0Cr decreases quickly during the initial tempering of 5 s to $(7.54 \pm 0.61) \times 10^{14} \text{ m}^{-2}$ and to $(6.31 \pm 0.64) \times 10^{14} \text{ m}^{-2}$, respectively. The slightly higher rate of decrease for the dislocation density in alloy 0.15C–4.0Cr may be caused by a higher strain energy stored, i.e., higher initial dislocation density in that alloy. After the initial decrease in the dislocation density, further reduction in the dislocation density in both alloys is much slower. After 5000-h tempering, the dislocation densities in alloys 0.15C–4.0Cr and 0.15C–1.0Cr are $(5.25 \pm 0.41) \times 10^{13}$ and $(3.64 \pm 0.14) \times 10^{13} \text{ m}^{-2}$, respectively. These values are slightly lower than the dislocation density ($6 \times 10^{13} \text{ m}^{-2}$) reported by Pešička et al. [14] in a P91 alloy after tempering at 750 °C for 100 h. The difference in

dislocation density between these alloys after long-term tempering could be ascribed to the difference in alloying elements, e.g., 7.38 wt% Cr in P91 alloy, heat treatment and/or the evaluation methods [14].

The dislocation densities of fresh martensite, evaluated for the two alloys in the present work, are compared to data from the literature in Fig. 3b [10, 21, 25–30]. It can be seen that the data from the present work are in good agreement with previous studies with similar carbon contents. It should, however, be mentioned that in addition to carbon, other alloying elements will also affect the dislocation density of martensite [9, 25, 28]. This is also seen in the present work where the high-Cr alloy has a slightly higher dislocation density than the low-Cr alloy in the as-quenched condition and is in agreement with our prior observations that Cr has a similar effect to C on the lath martensite microstructure [17]. It may be related to the slight lowering of the M_s temperature (Table 1) when the Cr content increases [14, 17]. It should also be noted that there is a difference in the prior austenite grain size between the two alloys of $40 \pm 6 \mu\text{m}$ for 4% Cr alloy and $65 \pm 8 \mu\text{m}$ for 1% Cr alloy [17]. Though it is generally believed that the prior austenite grain size affects the dislocation density of martensite, the difference in prior austenite grain size between the two alloys here is small and the effect of the difference due to alloying element content is believed to be larger [14, 17]. After long-term tempering, the dislocation density in

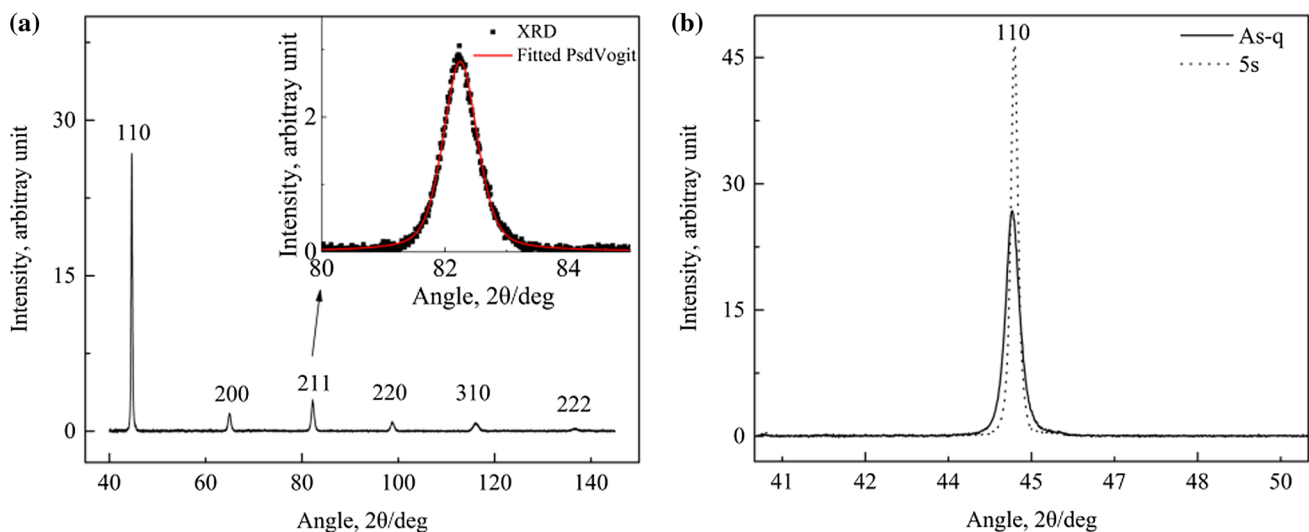


Figure 1 a XRD pattern of as-quenched 0.15C–4.0Cr alloy, inset shows the 211 peak fitted using a pseudo-Voigt function; b X-ray diffraction peak 110 for the 0.15C–4.0Cr alloy in as-quenched and 5 s at 700 °C tempered conditions.

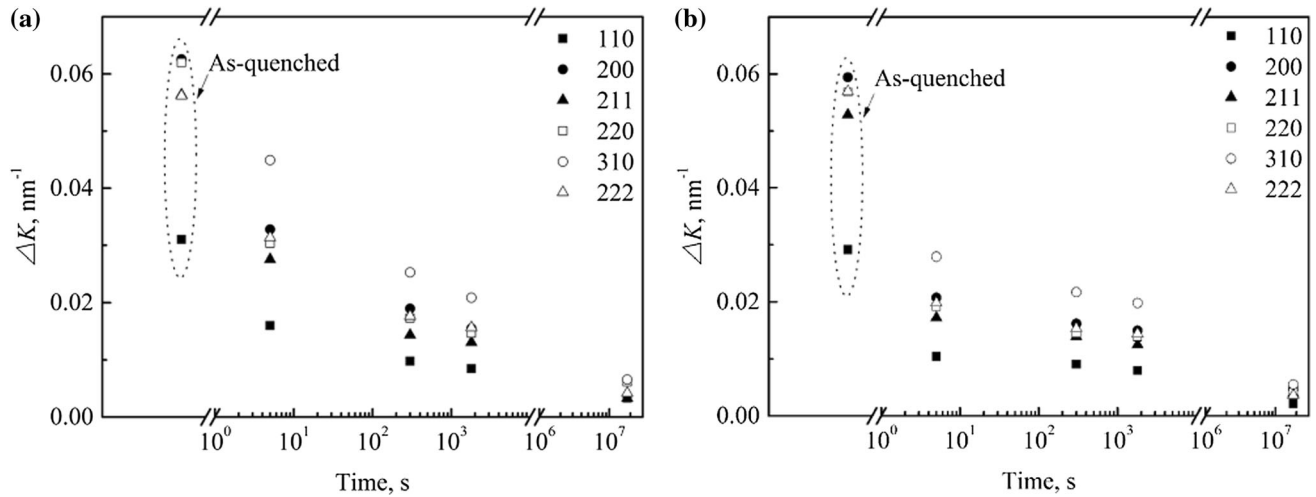


Figure 2 XRD peak broadening of each reflection defined by ΔK for as-quenched and tempered conditions of alloys 0.15C–4.0Cr (a) and 0.15C–1.0Cr (b).

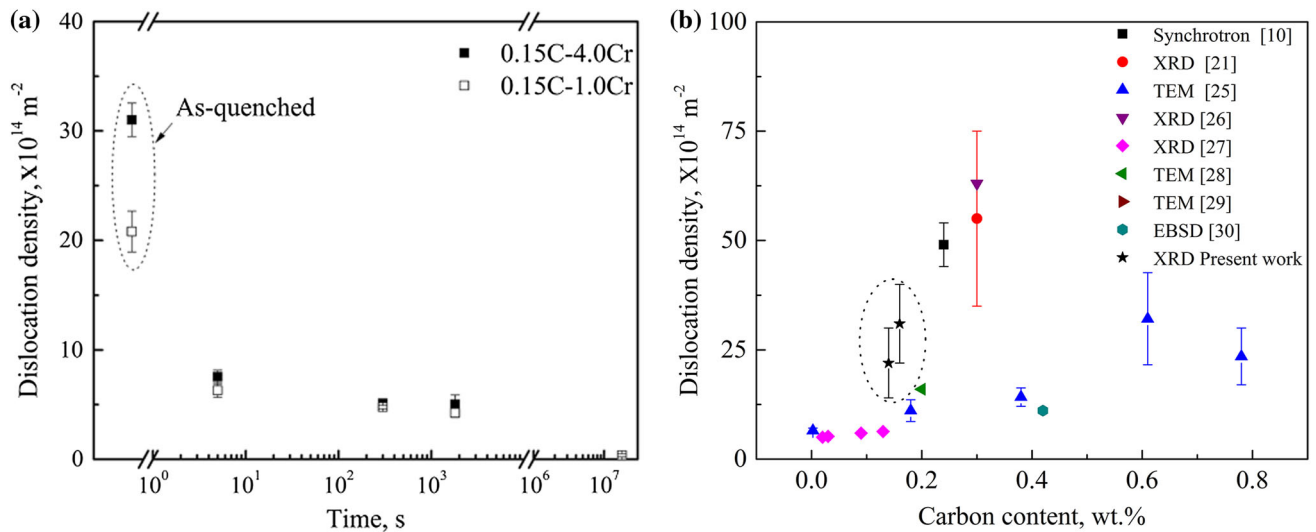


Figure 3 a Evolution of dislocation density in martensitic Fe–C–Cr alloys during tempering at 700 °C. b Dislocation density depending on carbon content of the steel alloys as compared with the literature data. Circled points in “b” are the values obtained in the present work.

the high-Cr alloy is slightly higher than that in the low-Cr alloy. It could be related to the difference in Cr content [14] although the difference in dislocation density between the two conditions is too small to draw any conclusion.

Table 2 shows the experimentally determined lattice parameters and the estimated carbon contents for the different conditions, i.e., as-quenched, room temperature aged and reference conditions. The evaluated interstitial solute carbon (C_{ss}) in the matrix phase is about 0.1–0.14 wt% in both alloys in the as-quenched condition, see Table 2. This indicates that all the carbon in the parent austenite phase is kept in

solid solution in the martensite after quenching. It should be noted, though, that if the martensite is kept at room temperature for an extended period, carbon will segregate and the lattice parameter (a_{As-q^t}) will be closer to the reference sample with an equilibrium amount of carbon in the martensite, see Table 2.

Microstructure evolution from ECCI and EBSD

In this section, the evolution of the hierarchical martensitic microstructure, consisting of fine laths, sub-blocks, blocks, packets and prior austenite grain

Table 2 Carbon in solid solution (C_{ss}) as determined from the lattice parameters of as-quenched (a_{As-q}), room temperature aged (a_{As-q*}) and reference conditions ($a_{Ref.}$) of the martensitic steels

| Samples | $a_{Ref.}$ (Å) | a_{As-q} (Å) | C_{ss} wt% | a_{As-q*} (Å) | C_{ss} wt%* |
|-------------|----------------|----------------|----------------------|-----------------|---------------------|
| 0.15C–4.0Cr | 2.8695 | 2.8739 | 0.1387 ± 0.0235 | 2.8708 | 0.0415 ± 0.0235 |
| 0.15C–1.0Cr | 2.8689 | 2.8724 | 0.09983 ± 0.0235 | 2.8701 | 0.0356 ± 0.0235 |

*Left at room temperature for 250 days

boundaries, is presented. The fine laths are about 50–100 nm thick, whereas the EBSD scan step size used in this study is of the same order. It could be possible to optimize the resolution of the EBSD and use a smaller step size, but the amount of time needed to capture a statistically populated set of data for lath thickness would be costlier in comparison with other competitive techniques like ECCI and TEM. Compared to the quantification of the thickness using TEM, the main advantage of ECCI is its capability to capture a large amount of laths in a quicker way. It has proven to be a powerful tool when combined with EBSD to evaluate microstructural parameters like misorientation distribution [31]. EBSD analysis was specifically used here to evaluate the “unit size” and to perform correlative work with ECCI so as to identify precipitation at certain boundaries. In the present work, the term “unit” represents regions separated by misorientation angles larger than 5° within a packet of martensite [32] in order to collectively specify features which are otherwise called by various names such as sub-block, block, domain and colony [14, 22, 23].

Figure 4 shows inverse pole figure (IPF) color-coded orientation maps of the as-quenched martensite in both alloys. The general microstructure is typical for fresh martensite in low carbon low alloy steels [23, 25, 28, 33]. A detailed explanation of the microstructural features can be found in Ref. [17].

Evolution of lath thickness

Figure 5a shows an example of the evaluation of the lath thickness by the line intercept method that was performed on ECCI micrographs. Examples of coarse and fine laths are shown in Fig. 5b. Thick laths of approximately $2.0 \mu\text{m}$ and thin laths of about $0.1\text{--}0.5 \mu\text{m}$ thickness are typically observed in the microstructure. It should be kept in mind that this is a 2D representation of a 3D microstructure, but within a packet where the laths align parallel to each other, it is believed to be a fair representation of the difference in lath thickness. Previous works using 3D data have revealed similar differences in coarseness of the martensite laths [33–35]. The potential change upon tempering was also investigated, and the results from

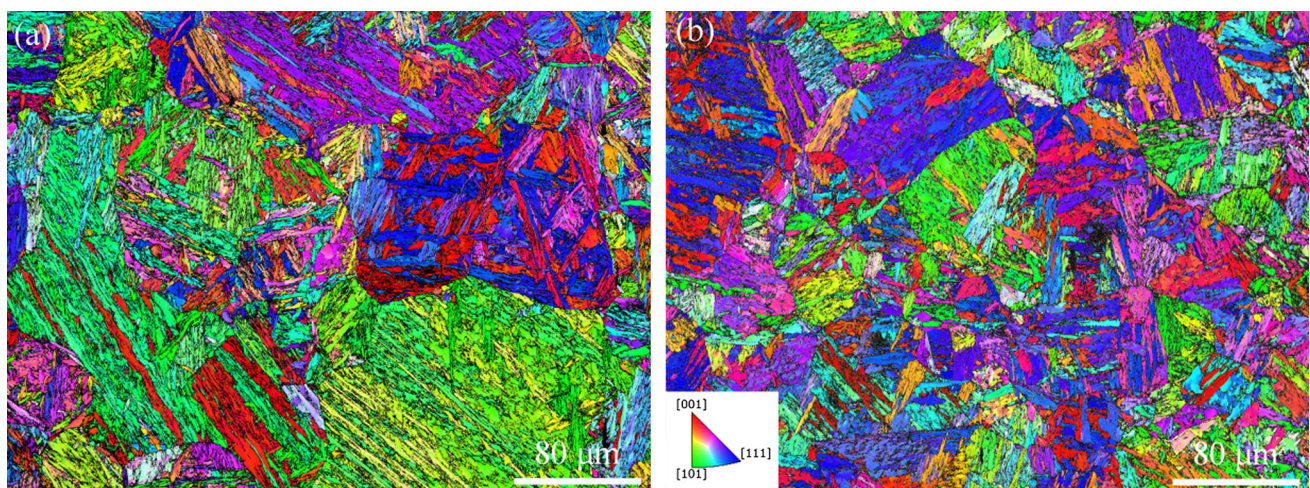
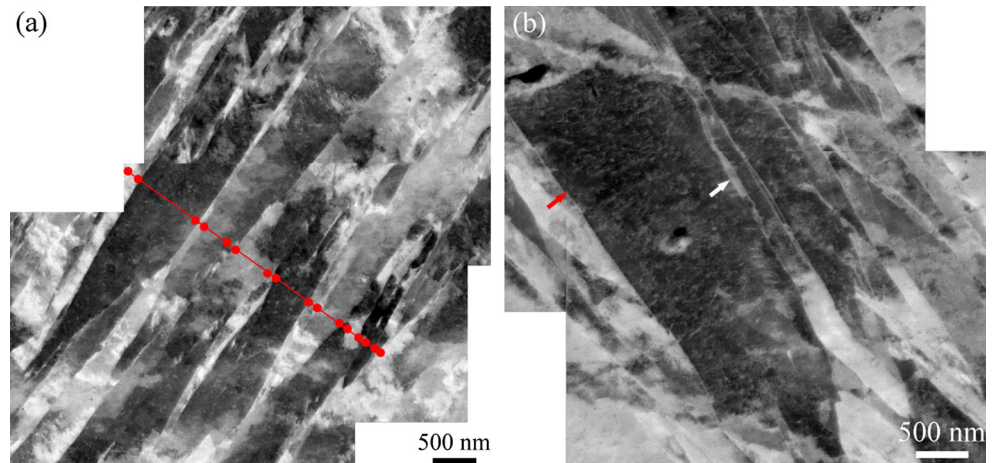
**Figure 4** Inverse pole figure color-coded maps of as-quenched microstructures of both alloys **a** 0.15C–4.0Cr; **b** 0.15C–1.0Cr obtained from SEM-EBSD. A standard stereographic triangle with colors indicating different orientations in the maps is given as inset.

Figure 5 ECCI micrographs of **a** martensite laths displaying the measurement of lath thickness by the line intercept method. A representative line (in red) and the intercepts are marked. **b** Heterogeneous nature of the martensitic microstructure: representations of a coarse lath (red arrow) and a thin lath (white arrow).



ECCI are shown in Fig. 6 together with results obtained from bright-field TEM images. The TEM and ECCI data are in good agreement, and the larger scatter of the ECCI data is due to the heterogeneity of the martensite lath thickness and the larger statistical sampling. Here, it should also be pointed out that the results shown in Fig. 6 might be a minor overestimation of the average lath thickness since it cannot be guaranteed that the contrast of laths in some cases is very similar making them virtually invisible. However, this effect is ensured to be minimal by applying a careful examination procedure.

Unit boundary evolution and influence of precipitates

When using standard grain boundary misorientation distribution plots for the EBSD data, as employed in

[23], it was not possible to identify any clear evolution of the boundaries in the present alloys with tempering. The martensite unit sizes in terms of their mean linear intercept lengths, where different misorientation criteria has been used to define the unit boundaries, could provide a better quantification method to distinguish these structures as suggested by Hutchinson et al. [23]. By employing this procedure, mean linear intercept values for misorientations larger than specific values were obtained for all samples. A typical micrograph with martensite packets and representative lines for the measurements is shown in Fig. 7a. Using this method, it was possible to identify differences in the evolution of size of the units, defined by different levels of misorientation. The mean linear intercept for units with high-angle boundaries (for example >15°) in

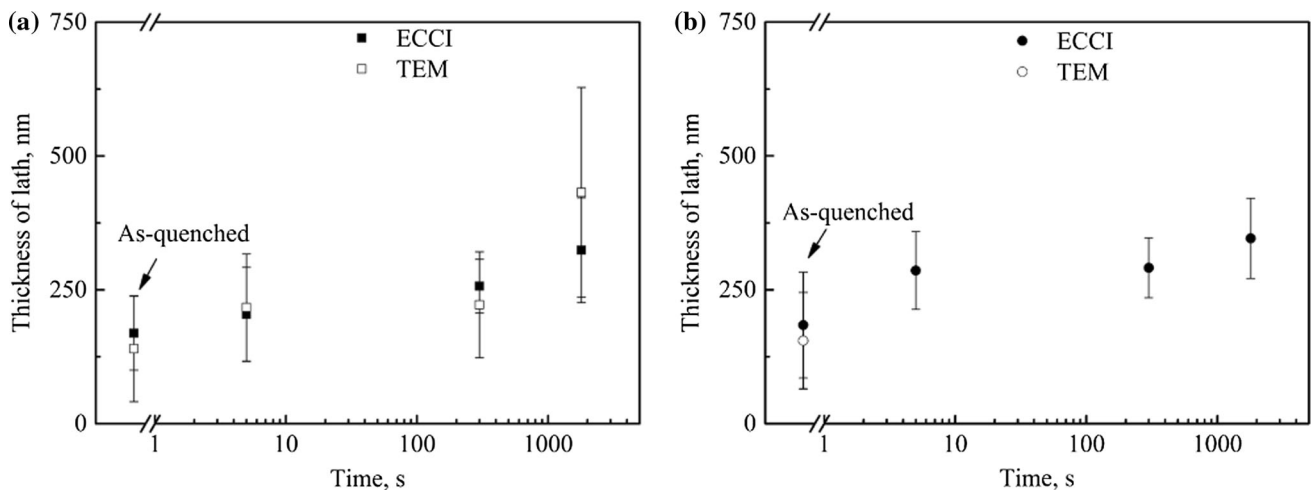


Figure 6 Variation in thickness of laths measured with TEM and ECCI images in the two alloys at the tested tempering durations. **a** 0.15C–4.0Cr; **b** 0.15C–1.0Cr.

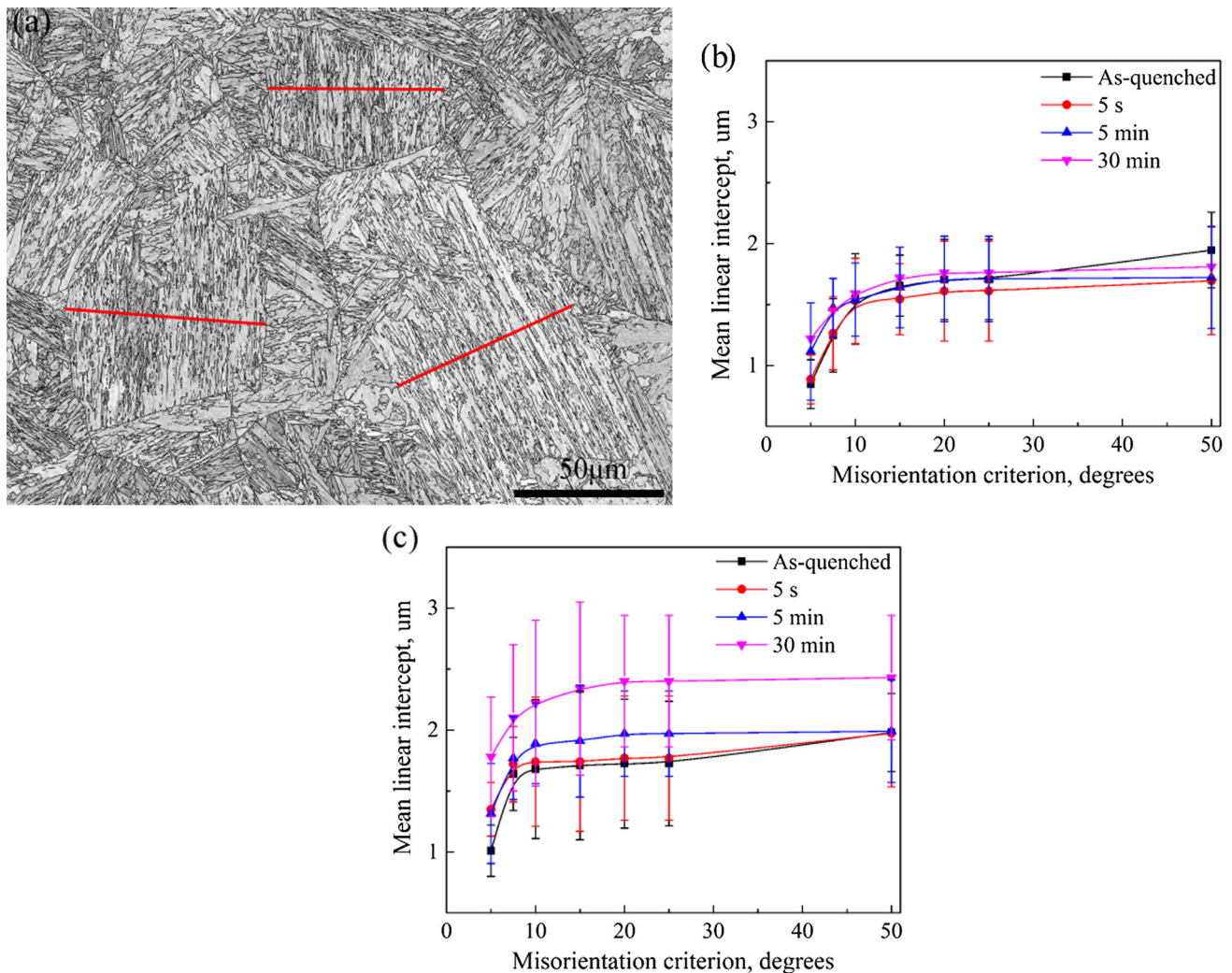


Figure 7 a EBSD pattern quality map overlaid with the unit boundaries (in black line) with misorientation $> 5^\circ$. The red lines indicate the way the line profiles were drawn to acquire misorientation profiles and the mean linear intercept lengths. b,

c illustrates the variation of the mean linear intercept lengths for different misorientation criteria in the as-quenched and tempered alloys: 0.15C-4.0Cr (b) and 0.15C-1.0Cr (c).

alloy 0.15C-4.0Cr is nearly constant among the tempered samples as shown in Fig. 7b; whereas in the alloy 0.15C-1.0Cr, the increase in mean linear intercept at different durations of tempering shows the increase in unit size after 5 min and 30 min of tempering, see Fig. 7c.

Figure 8 shows the ECCI micrographs of both alloys after 30-min tempering at 700 °C. The general lath martensitic microstructure in both alloys is similar to the as-quenched state, but the thickness of laths has increased (quantitatively seen in Fig. 6) and the shape of the laths are not as sharp, i.e., corners are rounded-off. From Fig. 8, it is further seen that the precipitates formed during tempering along the lath

and unit boundaries in 0.15C-4.0Cr are smaller and more numerous as compared to what is found in 0.15C-1.0Cr, see Fig. 8a, b. Obtaining this type of information on both the fine-scale lath microstructure and the distribution of nano-sized precipitates simultaneously is difficult in normal secondary electron imaging of SEM.

Figure 9 shows typical TEM bright-field images of precipitates together with their selected area electron diffraction (SAED) pattern and EDS spectrum in both samples. It was confirmed from SAED patterns that the precipitates in 0.15C-4.0Cr were mainly M_7C_3 while the precipitates in 0.15C-1.0Cr were mainly M_3C . The Cr content of M_3C , estimated using EDS

Figure 8 ECCI micrographs showing laths and precipitates in **a** 0.15C–4.0Cr; **b** 0.15C–1.0Cr after tempering for 30 min at 700 °C.

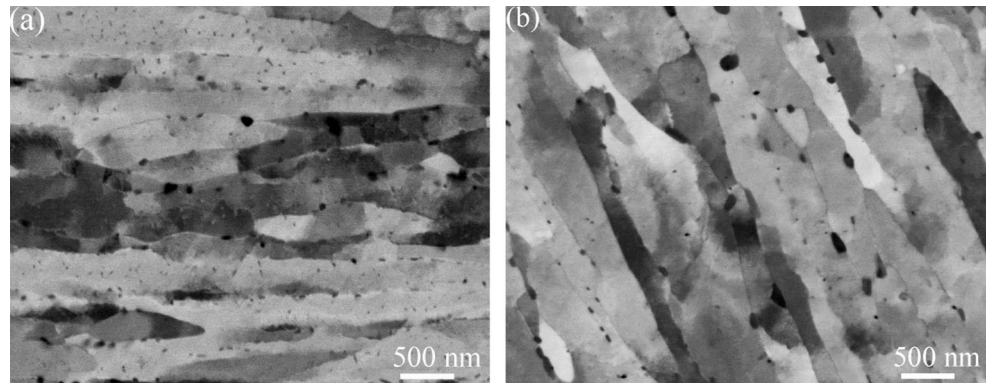
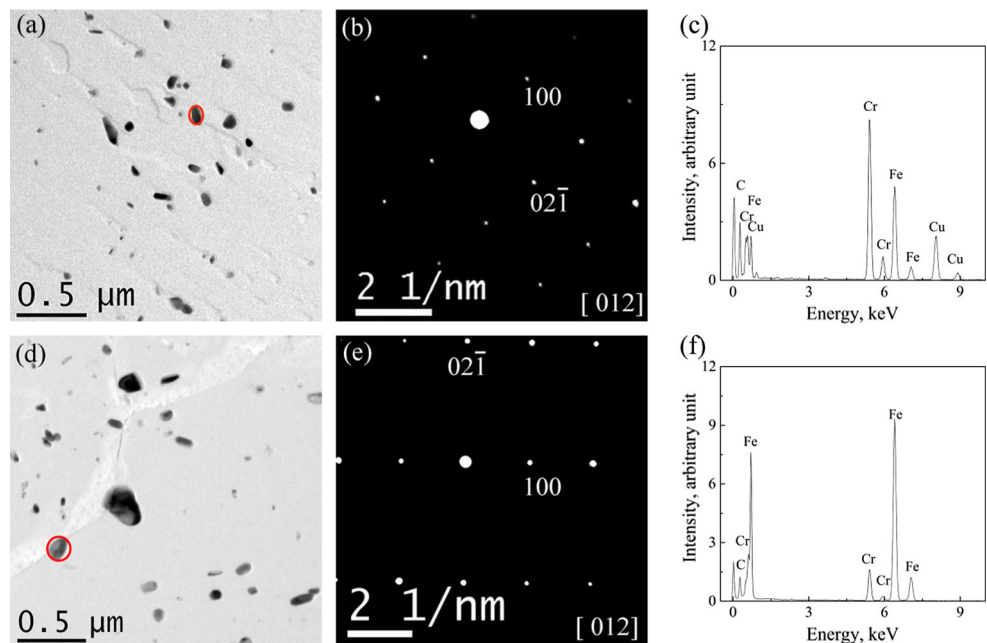


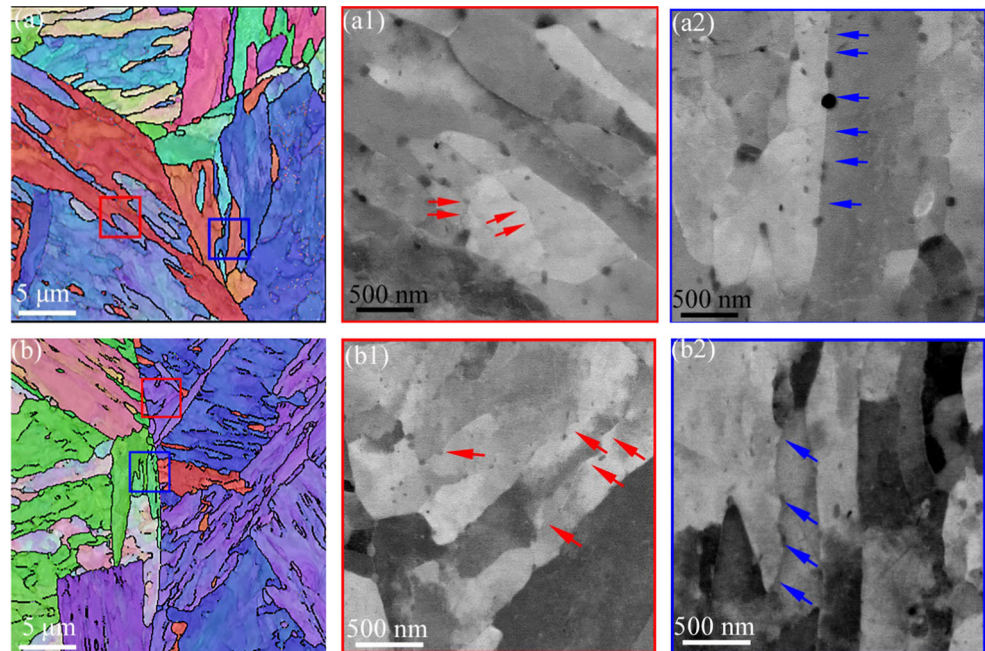
Figure 9 TEM bright-field image for precipitates (**a**, **d**), SAED pattern (**b**, **e**) and EDS spectrum (**d**, **f**) in **a–c** 0.15C–4.0Cr and **d–f** 0.15C–1.0Cr after tempering for 30 min at 700 °C. Red circles in the bright-field TEM images indicate the precipitates from which SAED patterns and EDS spectra were obtained. Zone axis of SAED patterns is noted in square brackets in (**b**) and (**e**).



analysis of the metallic elements and assuming stoichiometric C , is 11.8 wt%, while in M_7C_3 it is 55.5 wt%. The measured Cr content in both cases is lower than the equilibrium values which are 18.0 wt% in M_3C and 70.7 wt% in M_7C_3 . The size (radius) and number density of precipitates evaluated for alloy 0.15C–4.0Cr were 24.5 ± 3.1 nm and $(5.99133 \pm 0.55) \times 10^{12} \text{ m}^{-2}$ [24], and for alloy 0.15C–1.0Cr, they were 38.2 ± 4.6 nm and $(7.09 \pm 0.57) \times 10^{10} \text{ m}^{-2}$, respectively. It should be noted that observations of M_7C_3 in 0.15C–1.0Cr and $M_{23}C_6$ in 0.15C–4.0Cr were also made, but these precipitates were rare and can be considered of minor importance for the microstructure evolution. After tempering for 5000 h, only one type of precipitate was found in each alloy, i.e., M_7C_3 in alloy 0.15C–4.0Cr and M_3C in alloy 0.15C–1.0Cr.

A representative region from both alloys tempered for 30 min, where the effect of the precipitates on the coarsening of the microstructure is shown in Fig. 10. In both cases, lath boundaries are decorated with precipitates, but as seen in Fig. 10(b, b1, b2), some boundaries in alloy 0.15C–1.0Cr seem to bow out between precipitates (red and blue arrows), indicating coarsening of both the laths and the units. In contrast, the unit boundaries in alloy 0.15C–4.0Cr (blue arrows in Fig. 10a2) are mostly straight with precipitates densely populated along them. By collectively observing Figs. 8 and 10, it can be seen that the bowing of unit boundaries is heterogeneous within a specific alloy. However, after comparison of numerous micrographs of both alloys tempered for 30 min, we observe that the bowing of unit boundaries is more pronounced and the occurrence is more

Figure 10 Correlated EBSD–ECCI images in **a**, **a1** and **a2** for 0.15C–4.0Cr, and in **b**, **b1** and **b2** for 0.15C–1.0Cr after tempering for 30 min at 700 °C. Black lines in IPF **a**, **b** show the boundaries with misorientation > 5°. **a1**, **b1** and **a2**, **b2** are the areas marked by red and blue rectangles, respectively. The red and blue arrows represent the lath boundaries and “unit” boundaries, respectively.



frequent in the case of alloy 0.15C–1.0Cr, as compared to the 0.15C–4.0Cr alloy, where very few unit boundaries are bowing and the magnitude of the bowing is lower.

The observations of boundary pinning give an important clue about the precipitation event. In our previous work [24], a significant amount of precipitates was found in the microstructure for the same alloys after 5-s tempering. This means that the precipitates form early during microstructure coarsening. Thus, the difference in unit size evolution between the alloys considered in this study should depend on the precipitates type, size distribution, number density and their effectiveness in pinning the unit boundaries. The slower coarsening of the units in alloy 0.15C–4.0Cr as compared to alloy 0.15C–1.0Cr is most likely a result of pinning by the precipitates. Hence, these observations give an indication that the M_7C_3 precipitates found in alloy 0.15C–4.0Cr are more effective in pinning than the M_3C precipitates found in alloy 0.15C–1.0Cr. The recovery and dislocation annihilation are not expected to be affected significantly by the small precipitates at the early stages of aging as seen in [36].

The as-quenched martensitic microstructure usually contains a highly dense network of dislocations. During the initial stages of tempering these dislocations tend to recover and after prolonged tempering recrystallization of the microstructure occurs, a

process very much dependent on the alloy composition [1, 2, 37]. From the TEM and SEM microstructural observations, only dislocation recovery was found in all the stages of tempering in the two alloys discussed here. This is evidenced by (1) the stable dislocation density ($\sim 5 \times 10^{-14} \text{ m}^{-2}$) after about 30 min of tempering; (2) the rather stable distribution of misorientation angle boundaries, i.e., no newly formed high-angle grain boundary due to recrystallization; and (3) no visible appearance of equiaxed grains. The dislocation density even after 5000-h tempering is two orders of magnitude larger compared to the dislocation density of annealed cold-rolled steels (10^{10} to 10^{11} m^{-2}) [2]. It is often believed that the recrystallization could occur in low carbon (< 0.2 wt%) martensitic steels at 600–700 °C tempering, but not when alloying elements such as Mn, Cr are present [1, 5, 6]. However, recrystallization in steels containing extra-low/low carbon/medium carbon, tempered at 700 °C, has been reported previously [1, 37, 38]. The reason for these contradicting results in the literature is still unknown. In the present work, it can be speculated that the pinning effect of carbides on boundaries is high, and a large driving force is thus needed for recrystallization to occur. However, the sharp drop in dislocation density even after short-term tempering at 700 °C leads to a reduction in the driving force available for

recrystallization. This may explain why no recrystallization is observed here.

Conclusions

- The dislocation density of fresh martensite and martensite tempered at 700 °C has been investigated for two alloys: Fe–0.15C–(1.0, 4.0) Cr (wt%). The high dislocation density of the fresh martensite decreases rapidly during the initial tempering of 5 s but tempering beyond a few minutes does not further reduce the dislocation density significantly.
- The initial lath martensitic microstructures of both investigated alloys with coarse and fine laths coarsen slowly during tempering. However, a clear distinction between the low- and high-Cr alloys was found regarding the mobility of unit (high-angle) boundaries. In the low-Cr alloy, cementite forms and coarsens rapidly and thus causes little hindrance for coarsening of the units. On the other hand, in the high-Cr alloy, M_7C_3 forms more densely at unit boundaries and coarsens more slowly, leading to an effective pinning of the unit boundaries.

Acknowledgements

The work was performed within the VINN Excellence Center Hero-m, financed by VINNOVA, the Swedish Governmental Agency for Innovation Systems, Swedish industry and KTH Royal Institute of Technology. The authors are grateful to Fredrik Lindberg and Niklas Pettersson at Swerea KIMAB for experimental assistance, and to Lindsay Leach for valuable comments on the manuscript. Z. H. acknowledges the support from the China Scholarship Council (CSC), the National Natural Science Foundation of China (Nos. 51674080, 51404155, U1260204).

Compliance with ethical standards

Conflict of interest The authors declare that the contents have no conflict of interest toward any individual or organization.

Open Access This article is distributed under the terms of the Creative Commons Attribution 4.0 International License (<http://creativecommons.org/licenses/by/4.0/>), which permits unrestricted use, distribution, and reproduction in any medium, provided you give appropriate credit to the original author(s) and the source, provide a link to the Creative Commons license, and indicate if changes were made.

References

- [1] Krauss G (2017) Tempering of lath martensite in low and medium carbon steels: assessment and challenges. *Steel Res Int*. <https://doi.org/10.1002/srin.201700038>
- [2] Bhadeshia HKDH, Honeycombe SR (2006) The tempering of martensite, steels, 3rd edn. Butterworth-Heinemann, Oxford, pp 183–208
- [3] Speich GR (1973) Tempered ferrous martensitic structures, metallography, structures and phase diagrams. In: *Metals handbook*, 8th edn, vol 8, American Society for Metals, Metals Park, pp 202–204
- [4] Jack KH (1951) Structural transformations in the tempering of high carbon martensitic steels. *J Iron Steel Inst* 169:26–36
- [5] Speich GR (1972) Tempering of steel. *Metall Trans* 3(5):1043–1054
- [6] Caron RN, Krauss G (1972) The tempering of Fe–C lath martensite. *Metall Mater Trans A* 3(9):2381–2389
- [7] Ohmura T, Hara T, Tsuzaki K (2003) Evaluation of temper softening behavior of Fe–C binary martensitic steels by nanoindentation. *Scripta Mater* 49(12):1157–1162
- [8] Ohmura T, Tsuzaki K, Matsuoka S (2002) Evaluation of the matrix strength of Fe-0.4 wt% C tempered martensite using nanoindentation techniques. *Philos Mag A* 82(10):1903–1910
- [9] Kim B, Boucard E, Sourmail T, Martín DS, Gey N, Rivera-Díaz-del-Castillo PEJ (2014) The influence of silicon in tempered martensite: understanding the microstructure-properties relationship in 0.5–0.6 wt% C steels. *Acta Mater* 68:169–178
- [10] Saha DC, Biro E, Gerlich AP, Zhou Y (2016) Effects of tempering mode on the structural changes of martensite. *Mater Sci Eng A* 673:467–475
- [11] Ohlund CEIC, Lukovic M, Weidow J, Thuvander M, Offerman SE (2016) A comparison between ultra-high-strength and conventional high-strength fastener steels: mechanical properties at elevated temperature and microstructural mechanisms. *ISIJ Int* 56(10):1874–1883

- [12] Ohlund CEIC, Offerman SE, Schlangen E (2013) The kinetics of softening and microstructure evolution of martensite in Fe–C–Mn steel during tempering at 300 °C. *Mater Sci Eng A* 560:351–360
- [13] Xu LQ, Zhang DT, Liu YC, Ning BQ, Qiao ZX, Yan ZS, Li HJ (2014) Precipitation behavior and martensite lath coarsening during tempering of T/P92 ferritic heat-resistant steel. *Int J Min Metall Mater* 21(5):438–447
- [14] Pešička J, Kužel R, Dronhofer A, Eggeler G (2003) The evolution of dislocation density during heat treatment and creep of tempered martensite ferritic steels. *Acta Mater* 51(16):4847–4862
- [15] Zhang CY, Wang QF, Ren JX, Li RX, Wang MZ, Zhang FC, Yan ZS (2012) Effect of microstructure on the strength of 25CrMo48V martensitic steel tempered at different temperature and time. *Mater Des* 36:220–226
- [16] Allison J, Backman D, Christodoulou L (2006) Integrated computational materials engineering: a new paradigm for the global materials profession. *JOM* 58(11):25–27
- [17] Hou ZY, Hedström P, Xu YB, Wu D, Odqvist J (2014) Microstructure of martensite in Fe–C–Cr and its implications for modelling of carbide precipitation during tempering. *ISIJ Int* 54(11):2649–2656
- [18] Stormvinter A, Borgenstam A, Ågren J (2012) Thermodynamically based prediction of the martensite start temperature for commercial steels. *Metall Mater Trans A* 43(10):3870–3879
- [19] Hossein Nedjad S, Movaghar Gharabagh MR (2008) Dislocation structure and crystallite size distribution in lath martensite determined by X-ray diffraction peak profile analysis. *Int J Mater Res* 99(11):1248–1255
- [20] Schaffer E, Zehetbauer M, Ungár T (2001) Measurement of screw and edge dislocation density by means of X-ray Bragg profile analysis. *Mater Sci Eng A* 319–321:220–223
- [21] HajyAkbari F, Sietsma J, Böttger AJ, Santofimia MJ (2015) An improved X-ray diffraction analysis method to characterize dislocation density in lath martensitic structures. *Mater Sci Eng A* 639:208–218
- [22] Ungár T (2004) Microstructural parameters from X-ray diffraction peak broadening. *Scripta Mater* 51(8):777–781
- [23] Hutchinson B, Hagström J, Karlsson O, Lindell D, Tornberg N, Lindberg F, Thuvander M (2011) Microstructures and hardness of as-quenched martensites (0.1–0.5% C). *Acta Mater* 59(14):5845–5858
- [24] Hou ZY, Hedström P, Chen Q, Xu YB, Wu D, Odqvist J (2016) Quantitative modeling and experimental verification of carbide precipitation in a martensitic Fe–0.16 wt% C–4.0 wt% Cr alloy. *Calphad* 53:39–48
- [25] Morito S, Nishikawa J, Maki T (2003) Dislocation density within lath martensite in Fe–C and Fe–Ni alloys. *ISIJ Int* 43(9):1475–1477
- [26] Takebayashi S, Kunieda T, Yoshinaga N, Ushioda K, Ogata S (2010) Comparison of the dislocation density in martensitic steels evaluated by some X-ray diffraction methods. *ISIJ Int* 50(6):875–882
- [27] Cong ZH, Murata Y (2011) Dislocation density of lath martensite in 10Cr–5W heat-resistant steels. *Mater Trans* 52(12):2151–2154
- [28] Morito S, Yoshida H, Maki T, Huang X (2006) Effect of block size on the strength of lath martensite in low carbon steels. *Mater Sci Eng A* 438–440:237–240
- [29] Furuhashi T, Kobayashi K, Maki T (2004) Control of cementite precipitation in lath martensite by rapid heating and tempering. *ISIJ Int* 44(11):1937–1944
- [30] Revilla C, López B, Rodríguez-Ibabe JM (2014) Carbide size refinement by controlling the heating rate during induction tempering in a low alloy steel. *Mater Des* 62:296–304
- [31] Borrajo-Pelaez R, Hedström P (2017) Recent developments of crystallographic analysis methods in the scanning electron microscope for applications in metallurgy. *Crit Rev Solid State Mater Sci*. <https://doi.org/10.1080/10408436.2017.1370576>
- [32] Morito S, Adachi Y, Ohba T (2009) Morphology and crystallography of sub-blocks in ultra-low carbon lath martensite steel. *Mater T JIM* 50(8):1919–1923
- [33] Morsdorf L, Tasan CC, Ponge D, Raabe D (2015) 3D structural and atomic-scale analysis of lath martensite: effect of the transformation sequence. *Acta Mater* 95:366–377
- [34] Rowenhorst DJ, Guptab A, Feng CR, Spanos G (2006) 3D Crystallographic and morphological analysis of coarse martensite: combining EBSD and serial sectioning. *Scripta Mater* 55:11–16
- [35] Hedström P, Stormvinter A, Borgenstam A, Gholinia A, Winiarski B, Withers PJ, Karlsson O, Hagström J (2012) In: 1st international conference on 3D materials science, TMS 2012, p 19
- [36] Roumina R, Sinclair CW (2010) Recovery kinetics in the presence of precipitates: the softening response of an Al–Mg–Sc alloy. *Acta Mater* 58:111–121
- [37] Samuel FH, Hussein AA (1983) A comparative study of tempering in steel. *Mater Sci Eng A* 58(1):113–120
- [38] Tschiyama T, Miyamoto Y, Takaki S (2001) Recrystallization of lath martensite with bulge nucleation and growth mechanism. *ISIJ Int* 41(9):1047–1052